A validation study of a bounce-averaged kinetic electron model in a KSTAR L-mode plasma ⊘

Sumin Yi ✉ ⓘ ; C. Sung ⓘ ; E. S. Yoon ⓘ ; Jae-Min Kwon ⓘ ; T. S. Hahm ⓘ ; D. Kim; J. Kang ⓘ ;
Janghoon Seo ⓘ ; Y. W. Cho ⓘ ; Lei Qi ⓘ

Check for updates

View Online   Export Citation   CrossMark

AIP Publishing

A validation study of a bounce-averaged kinetic electron model in a KSTAR L-mode plasma

View Online   Export Citation   CrossMark

Sumin Yi,[1,a] (iD) C. Sung,[2] (iD) E. S. Yoon,[3] (iD) Jae-Min Kwon,[1] (iD) T. S. Hahm,[4] (iD) D. Kim,[2] (iD) J. Kang,[1] (iD)
Janghoon Seo,[1] (iD) Y. W. Cho,[5] (iD) and Lei Qi[1] (iD)

AFFILIATIONS

[1]Korea Institute of Fusion Energy, Daejeon 34133, Republic of Korea
[2]Korea Advanced Institute of Science and Technology, Daejeon 34141, Republic of Korea
[3]Department of Nuclear Engineering, Ulsan National Institute of Science and Technology, Ulsan 44919, Republic of Korea
[4]Nuclear Research Institute for Future Technology and Policy, Seoul National University, Seoul 08826, Republic of Korea
[5]School of Physical and Mathematical Sciences, Nanyang Technological University, Singapore, Singapore

[a]Author to whom correspondence should be addressed: yism@kfe.re.kr

ABSTRACT

We extend the bounce-averaged kinetic (BK) electron model to be applicable in general tokamak magnetic geometries and implement it on the global δf particle-in-cell gyrokinetic code gKPSP. We perform a benchmark study of the updated BK model against the gyrokinetic electron model in flux-tube codes, CGYRO and GENE. From the comparisons among the simulations based on the local parameters of a KSTAR L-mode plasma, we confirm a reasonable agreement among the linear results from the different codes. In the nonlinear gKPSP simulation with a narrow plasma gradient region whose width comparable to the mode correlation length, ion and electron heat fluxes are compatible with those calculated by CGYRO. However, with an unstable region sufficiently wider than the mode correlation length, gKPSP predicts 2–3 times larger turbulent heat fluxes. Taking into account the differences between the flux-tube and global simulations, the overall agreement is encouraging for further validation and development of the BK electron model. In global simulations using a wide range of the experimental plasma profiles, we find an intricate coupling of turbulence spreading and a zonal flow in determining the radial profiles of turbulent heat fluxes, which has not been reported to date.

I. INTRODUCTION

Numerical modeling of microturbulence in magnetically confined plasmas has been advanced by the reduced kinetic descriptions relying on adiabatic invariants. The ion magnetic moment μ_i, the so-called first adiabatic invariant, is conserved for microinstabilities whose frequencies are lower than the ion gyrofrequency ω_{ci}. The gyrokinetic theory reduces the number of phase-space variables by applying the gyrocenter transform and eliminating the gyrophase dependency in phase-space Lagrangian.[1,2] In addition, considering a bounce motion of a particle trapped in a weak magnetic field region, the action associated with the bounce motion becomes the second adiabatic invariant. The bounce-averaged kinetic (BK) equations can be formulated by the transformation to the action-angle coordinate.[3,4] Treating the phase of the bounce motion as an ignorable coordinate, the BK model provides the reduced description of the bounce-center motion.

Although electron dynamics is described by the gyrokinetic equations in recent turbulence simulations,[5–7] it requires demanding computational resources. When one considers turbulence driven by trapped electron modes (TEMs), which are drift waves excited by the resonance with the toroidal precession of trapped electrons, the BK model is an efficient method of dealing with trapped electrons. An applicable situation is core transport of L-mode plasmas where ion temperature gradient-driven (ITG) modes and TEMs are considered to be dominant instabilities. Thus, the BK electron model can be a practical tool for modeling L-mode plasma transport in large tokamaks such as ITER. The BK electron model has been implemented on gyrokinetic codes, GT3D[8] and gKPSP,[9,10] for the description of kinetic electrons. Particularly, the gKPSP code has extensively exploited the BK electron model for researching TEM turbulence.[11,12] In gKPSP simulations, the computational cost for adding kinetic trapped electrons is limited to only 2–3 times of the simulation cost with adiabatic electrons. This efficient numerical scheme facilitates the exploration of a broad parameter range where a transition between ITG-dominant and TEM-dominant turbulence occurs.[12] However, the BK equations

04 March 2024 04:47:30

implemented in the aforementioned simulation codes are derived for analytic magnetic geometries. Because of this constraint, no validation study of the BK electron model involving experimental data has been conducted.

In this work, we extend the BK electron model in the gKPSP code for its application in experimental magnetic geometries. Then, we simulate a KSTAR L-mode plasma by using the extended BK model and compare our results to those obtained from the well-established full gyrokinetic codes, CGYRO[5] and GENE,[6] for validation purpose. Although validation is commonly defined as the process of determining the accuracy of a model compared to experimental data,[13] it is more difficult for the BK electron model to produce simulations consistent with experiment results than the gyrokinetic model. Thus, we construct an intermediate step of testing how faithfully the BK electron model represents interactions between trapped electrons and waves. In this sense, the gyrokinetic electron model serves as a good benchmark since it describes electron dynamics more precisely. In the previous studies, the BK electron model has already been confirmed to yield linear results very similar to the drift-kinetic model in analytic circular magnetic geometries.[8,9] In this study, expanding the benchmark exercise to experimental magnetic geometries, we confirm a reasonable agreement between the BK and gyrokinetic electron models. We find some discrepancies as well, identifying issues in the approximations in our BK electron model.

Even though gKPSP is a global code, the benchmark simulations are focused at a radial location since the benchmark results are obtained from radially local, flux-tube simulations. In the local approach, by assuming a disparate-scale separation between turbulence and equilibrium profiles, radial equilibrium profile variations are neglected. This promotes the numerical implementation of the full gyrokinetic equation system including gyrokinetic electrons and electromagnetic effects, so that flux-tube codes are widely used in turbulent transport modeling. However, the flux-tube approximation is in principle justified in the limit of $\rho_i/a \to 0$, where ρ_i and a are the ion gyroradius and the minor radius of a tokamak, respectively. For medium-sized tokamaks, e.g., KSTAR, one has to take into account the radial profile variations and thus the dynamics of mesoscale structures such as zonal flows[14] and heat flux avalanches.[15] These mesoscale phenomena are well-represented by global simulations. Furthermore, some simulated results from global codes are in better agreement with experimental data than local simulations, albeit validation studies employing global codes are rare.[16–18] For example, a validation work of ASDEX Upgrade plasmas by using both the local and global versions of the GENE code reported that the global simulations produce the ion and electron heat fluxes compatible with the experiments for the wide radial domain.[17] However, it was found that the local GENE simulations lead to an overestimation of the experimental heat fluxes at outer radii. In this work, motivated by the reasonable validity of the BK electron model in the gKPSP code, we further investigate characteristics of global simulations by taking the experimental profiles in a wide radial range. We find an interesting effect of mesoscale transport phenomena in determining radial profiles of turbulent heat fluxes.

The remainder of this paper is organized as follows: In Sec. II, the basic equations in the BK electron model are given. In Sec. III, we introduce the KSTAR plasma studied in this work. We present numerical results that examine the validity of our model and the characteristics of global simulations in Secs. IV and V, respectively. Finally, we draw conclusions with discussions in Sec. VI.

II. THE SIMULATION METHOD: BOUNCE-AVERAGED KINETIC ELECTRON MODEL

We consider the axisymmetric equilibrium magnetic field given by $\mathbf{B} = \nabla\alpha \times \nabla\psi$, where α and ψ are the field line label and poloidal magnetic flux, respectively. Denoting the distance along the field line by ℓ, the lowest-order equations of motion for trapped electrons parallel to the magnetic field are given by

$$\frac{d\ell}{dt} = v_\parallel, \tag{1}$$

$$\frac{dv_\parallel}{dt} = -\mu_e \frac{\partial B}{\partial \ell}, \tag{2}$$

where $v_\parallel$ is the parallel velocity at a point on a trapped electron's bounce orbit and $\mu_e = m_e v_\perp^2/(2B)$ the electron magnetic moment with m_e being the electron mass. We can define the action-angle variables for this periodic bounce motion as

$$J(\psi, E_0, \mu_e) = \frac{1}{\pi} \int_{\ell_0}^{\ell_1} m_e |v_\parallel| d\ell, \tag{3}$$

$$\Psi(\psi, \ell, E_0, \mu_e) = \pi + \omega_b \int_{\ell_0}^{\ell} \frac{d\ell'}{|v_\parallel|}. \tag{4}$$

Here, $E_0 = m_e v_\parallel^2/2 + \mu_e B$ is the energy and $\omega_b = \partial H_0(\psi, J, \mu_e)/\partial J$ is the bounce angular frequency defined with the unperturbed Hamiltonian in terms of J. The coordinate transform $(\ell, v_\parallel) \to (J, \Psi)$ and the elimination of the bounce-angle dependency in the phase-space Lagrangian lead to the BK equations.[4] The evolution of the bounce-center distribution function $F_e(\psi, \alpha, J, \mu_e)$ in the bounce-center coordinate is given by

$$\frac{\partial F_e}{\partial t} + \frac{d\psi}{dt}\frac{\partial F_e}{\partial \psi} + \frac{d\alpha}{dt}\frac{\partial F_e}{\partial \alpha} = 0, \tag{5}$$

where the bounce-averaged equations of motion are

$$\frac{d\psi}{dt} = c\frac{\partial \langle \delta\phi \rangle_b}{\partial \alpha}, \tag{6}$$

$$\frac{d\alpha}{dt} = \frac{c}{e}\frac{\partial H_0}{\partial \psi} - c\frac{\partial \langle \delta\phi \rangle_b}{\partial \psi}. \tag{7}$$

Here, $\langle \delta\phi \rangle_b = \oint \delta\phi d\Psi/2\pi$ denotes the bounce average of the perturbed electrostatic potential $\delta\phi$, c the speed of light, and e the elementary charge. Note that the bounce-center coordinate adopted in our BK model is the lowest-order approximation retaining the parallel motion only. It is assumed that the guiding center is tied up to a given field line, i.e., the width of the bounce orbit vanishes. In addition to the fast parallel motion, the guiding center undergoes the slow perpendicular magnetic drifts across field lines. The "true" bounce-center coordinates at the order $\epsilon_k = k_\perp w_{b\sigma}$ include the corrections for the deviations from the given field line caused by the perpendicular drifts.[3] Here, $w_{b\sigma}$ is the bounce orbit width of a plasma species σ, where $\sigma = i\,(e)$ for the main ions (electrons). For trapped electrons experiencing TEM turbulence, $\epsilon_k \leq w_{be}/\rho_s \sim \sqrt{m_e/m_i}qR_0/r$ would be small enough to neglect its correction. Here, $\rho_s = c_s/\omega_{ci}$ is a reference gyroradius defined with the ion sound speed $c_s = \sqrt{T_e/m_i}$ and the ion gyrofrequency $\omega_{ci} = Z_i eB_0/(m_i c)$ with Z_i being the main ion charge number. B_0, R_0, r, and q are the magnetic field strength and the major radius at

the magnetic axis, a minor radius of a bounce orbit, and the safety factor, respectively. The approximate BK model in Eqs. (5)–(7) is practical for simulation applications and the assessment of its validity and limitations.

For the numerical implementation of the BK electron model, the evaluation of the radial derivative of $H_0(\psi, J, \mu_e)$ in terms the bounce-center coordinate is necessary. In the previous BK electron models, the H_0 expressions are derived for analytic tokamak equilibria. In the deeply trapped electron limit with $J \ll 1$, an approximate formula is given by[9,10]

$$H_0(\psi, J, \mu_e) = \mu_e B_0 \left(1 + \Delta - \varepsilon + \frac{\kappa_e^2}{2q^2}\varepsilon \right) + \frac{\sqrt{\varepsilon \mu_e B_{\min}}}{qR_0\sqrt{m_e}} J, \quad (8)$$

where $B_{\min}$ is the minimum magnetic field of the trapped electron orbit, Δ the Shafranov shift, κ_e elongation, and $\varepsilon = r/R_0$ the inverse aspect ratio. Later, the BK model is extended to arbitrary J by including H_0 of barely trapped electrons[19]

$$h_{barely}(\psi, J, \mu_e) = \mu_e B_{\max} + 4\omega_{b*}J_* \int_0^{(1-J/J_*)/4} \frac{du}{W_m(-u)}, \quad (9)$$
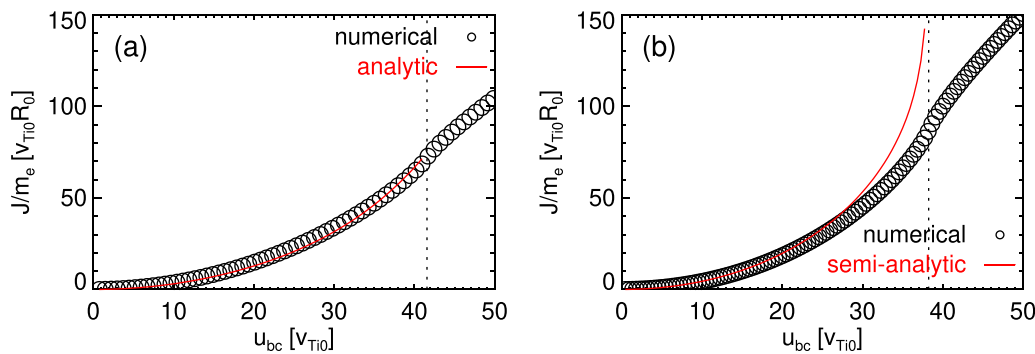
where $J_* = \frac{8}{\pi}qR_0\sqrt{m_e \varepsilon \mu_e B_0}$, $\omega_{b*} = \frac{\pi}{qR_0}\sqrt{\varepsilon \mu_e B_0/m_e}$, and $B_{\max}$ is the maximum magnetic field of the barely trapped electron orbit. Here, $W_m(y)$ is the second branch of Lambert function defined by $W(y)e^{W(y)} \equiv y$ for $W(y) < -1$.[20]

However, the BK equations derived for analytic tokamak equilibria are not suitable for experimental magnetic geometries, which are numerically calculated. To accommodate equation-free general tokamak magnetic geometries, we evaluate $\partial H_0(\psi, J, \mu_e)/\partial\psi$ in Eq. (7) numerically. For an experimental magnetic equilibrium given by $\psi(R, Z)$ in the cylindrical coordinate, J in Eq. (3) is written as

$$J(\psi, u_{bc}, \mu_e) = \frac{1}{\pi}\int_{\theta_0}^{\theta_1} m_e|v_\parallel| \frac{B}{B_p}\frac{r|\nabla\psi|}{|\mathbf{r}\cdot\nabla\psi|}rd\theta, \quad (10)$$

where (r, θ) is the geometrical polar coordinate, the poloidal magnetic field strength $B_p = |\nabla\psi|/R$, and

$$\frac{r|\nabla\psi|}{|\mathbf{r}\cdot\nabla\psi|} = \sqrt{\left(\frac{\partial\psi}{\partial R}\right)^2 + \left(\frac{\partial\psi}{\partial Z}\right)^2} \Big/ \left| \cos\theta\frac{\partial\psi}{\partial R} + \sin\theta\frac{\partial\psi}{\partial Z} \right|. \quad (11)$$

Here, we use u_{bc} as the velocity space variable instead of E_0, where u_{bc} is $v_\parallel$ at B_{min}. We calculate the J values on the (ψ, u_{bc}, μ_e) grid by integrating Eq. (10) numerically along the orbits of the particles on the grid points. Figure 1 shows J as a function of u_{bc} with $x = 0.58$ and $\mu_e = 0.7T_i(0)/B_0$, where $T_i(0)$ is the ion temperature at the magnetic axis. Here, $x = \sqrt{\psi/\psi_1}$ is the radial coordinate of the gKPSP code with ψ_1 being the poloidal magnetic flux on the last closed-flux surface. For the circular plasma based on the CYCLONE base case where an analytic magnetic equilibrium is employed in Fig. 1(a), we confirm that the numerically calculated J agrees well with the analytic expression[21]

$$J = J_*[E(\kappa) - (1 - \kappa^2)K(\kappa)]. \quad (12)$$

Here, $K(\kappa)$ and $E(\kappa)$ are complete elliptic integrals of the first and second kinds, respectively, and $\kappa^2 = u_{bc}^2/2\varepsilon v_{\perp,bc}^2$ is pitch angle at $B_{\min}$. Figure 1(b) corresponds to the KSTAR plasma, which will be introduced in Sec. III. In this case, we make a comparison with the semi-analytic expression valid in the deeply trapped electron limit, which is given by

$$J = \frac{m_e u_{bc}^2}{2\omega_b(\psi, u_{bc}, \mu_e)}. \quad (13)$$

Here, $\omega_b(\psi, u_{bc}, \mu_e)$ is numerically calculated. We confirm a good agreement between the two results in the small J limit, ensuring the accuracy of the numerical integration of J.
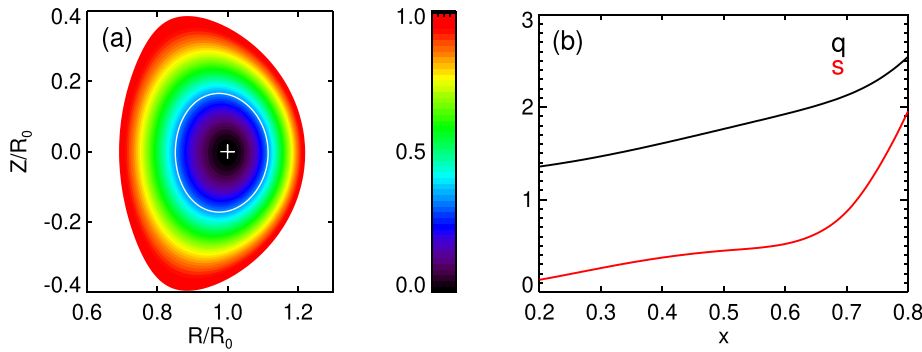
Now, we can find u_{bc} assigning J for given ψ and μ_e values from the constructed numerical function $J(\psi, u_{bc}, \mu_e)$. Then, H_0 in the bounce-center coordinate (ψ, J, μ_e) is given by

$$H_0(\psi, J, \mu_e) = \mu_e B_{min}(\psi) + \frac{1}{2}m_e u_{bc}^2(\psi, J, \mu_e). \quad (14)$$

We discretize H_0 by employing the finite element method. Details are given in the Appendix. We implement this BK electron model for general tokamak magnetic geometries in the gKPSP code. Other details of the BK electron model in the gKPSP code are presented in Refs. 9 and 10.

III. THE KSTAR PLASMA

TEM-dominant plasmas with a magnetic equilibrium reconstruction and plasma profile diagnostics are suitable for validating the BK

FIG. 1. Action J as a function of the parallel velocity of a trapped electron at its bounce center u_{bc} with $x = \sqrt{\psi/\psi_1} = 0.58$ and $\mu_e = 0.7T_i(0)/B_0$ for analytic circular (a) and experimental KSTAR magnetic geometries (b). The vertical lines denote the trapped-passing boundaries.

FIG. 2. (a) Normalized equilibrium poloidal magnetic flux in the (R, Z) plane for the plasma at 2050 ms in the KSTAR discharge #21631. The white ellipse indicates the radius $x = 0.58$ where a benchmark test is performed. (b) Safety factor and magnetic shear as a function of the radial coordinate $x = \sqrt{\psi/\psi_1}$.

electron model. Recently, the KSTAR L-mode discharge #21631 has been studied. Equilibrium magnetic reconstruction, kinetic profile, and transport analyses as well as uncertainty quantification have been systematically conducted in the previous work.[22] Note that carbon impurity with the constant $Z_{\text{eff}} = 2$ is assumed because impurity measurements were not available. Furthermore, the gyrokinetic analysis has revealed that the most unstable microinstability in the plasma at 2050 ms is TEM.[22] Thus, the previous work provides a favorable test case for the validation of the BK electron model. In this study, we investigate this plasma by using the gKPSP code with the BK electron model by adopting the experimental equilibrium data in the previous work. A brief overview of the L-mode discharge is as follows. Subjected to a toroidal magnetic field on the axis of $B_T = 2.5$ T, the plasma carrying a plasma current of $I_p = 600$ kA was heated by 2.9 MW of neutral beam injection. An up-down symmetric-shaped plasma is configured by an inboard limiter. The plasma at 2050 ms has the shape parameters of elongation $\kappa_e = 1.46$ and triangularity $\delta_t = 0.245$ at the last closed-flux surface. The major and minor radii of the plasma are $R_0 = 1.83$ m and $a = 0.48$ m, respectively. Figure 2 shows the normalized equilibrium poloidal magnetic flux ψ/ψ_1 on the (R, Z) plane and the safety factor q and the magnetic shear $s \equiv (x/q)(dq/dx)$ as a function of gKPSP's radial coordinate $x = \sqrt{\psi/\psi_1}$. Figure 3 displays the equilibrium density n_σ and temperature T_σ profiles of the main ions, electrons, and carbon impurities as well as their gradient profiles. Here, we define the inverse gradient scale lengths as $\frac{1}{\Lambda_Y} = -\frac{1}{Y}\frac{dY}{dx}$, where Y stands for density or temperature of a plasma species σ and $\sigma = C$ for the carbon impurities.

IV. VALIDATION SIMULATIONS

In this section, we present the benchmark results of the gKPSP simulations utilizing the BK electron model against the full gyrokinetic simulations. For the benchmark data, we take the previous gyrokinetic analysis results of the KSTAR plasma,[22] which is obtained by the electromagnetic δf flux-tube code CGYRO.[5] It should be noted that there are definite differences in numerical methods employed in flux-tube and global codes, e.g., treatment of radial equilibrium profile variations, radial discretization of fluctuations, boundary conditions, etc. Nevertheless, results from local and global simulations qualitatively agree. Regarding linear simulation results, their quantitative differences are usually not large. One example is found from the comparison of the local and global GENE simulations in Fig. 6 in Ref. 23. The linear flux-tube simulations exhibit growth rates only about 20% higher than the global results, while the frequencies from the local and global simulations are in good agreement. In this regard, the local results can serve as a fairly good benchmark standard, immediately available. The radial location where the previous CGYRO simulations were conducted is $r_{\text{ref}}/a = 0.5$, translated to $x_{\text{ref}} = 0.58$ in the gKPSP code. The simulated plasma is composed of deuteriums as the main ion species, electrons, and carbon impurities with the flat $Z_{\text{eff}} = 2.0$ profile. At $x = x_{\text{ref}}$, the electron density and temperature read $n_e = 2.52 \times 10^{19}$ m^{-3} and $T_e = 1.49$ keV, respectively. The density and temperature ratios of the ion species to electron are as follows: $n_i/n_e = 0.80$, $n_C/n_e = 0.03$, $T_i/T_e = 1.12$, and $T_C/T_e = 1.17$. The local values of the inverse gradient scale lengths are $\Lambda_{Te}^{-1} = 2.24$, $\Lambda_{Ti}^{-1} = 1.40$, $\Lambda_{TC}^{-1} = 1.52$, and $\Lambda_{ne}^{-1} = 1.79$. The local safety factor is $q = 1.89$ with the magnetic shear $s = 0.46$.
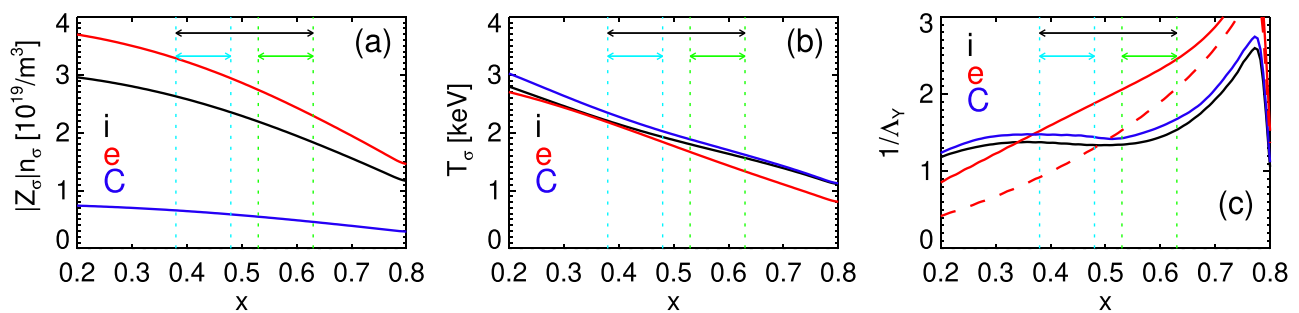
FIG. 3. Densities (a) and temperatures (b) as a function of the radial coordinate $x = \sqrt{\psi/\psi_1}$. (c) Inverse gradient scale lengths of density (dashed) and temperature (solid). Profiles of ions (black), electrons (red), and carbon impurities (blue) are displayed. The horizontal arrows represent the radial ranges employed in gKPSP simulations.

The gKPSP code describes the dynamics of the ion species by using the gyrokinetic equations. For trapped electrons, we use the BK model in Sec. II. Passing electrons are assumed to respond adiabatically. The self-consistent perturbed electrostatic potential is determined by the gyrokinetic Poisson equation. The Coulomb collisions between the ion species are modeled by a linearized collision operator with energy and momentum conserving terms.[24] The collisions for electrons are assumed to be dominated by pitch angle scattering against ions and replicated by the Lorentz operator.[25] For the details of the simulation model and numerical methods in the gKPSP code, we refer Refs. 9,10, and 26. We take into account neither an equilibrium radial electric field $E_{r,eq}$ nor fast ions to focus on discrepancies, if any, caused by the BK electron model. We posit that electromagnetic effects are negligible because of the low plasma beta value as $\beta_e = 8\pi n_e T_e/B_0 = 0.3\%$ at $x = x_{\rm ref}$.

gKPSP simulations employ the following numerical parameters. As a baseline case, we take the experimental plasma profiles within the narrow radial range $x = 0.53 - 0.63$, marked by the green arrows in Fig. 3, corresponding to the width of the plasma gradient region $W = 0.1$. Simulated is half of the torus containing 48 toroidal modes. The toroidal mode spectrum covers up to $k_\theta \rho_s = 1.79$ with $dk_\theta \rho_s = 0.038$. In this section, ρ_s and c_s correspond to the local values at $x = x_{\rm ref}$. We set the radial grid size to $dx \approx 0.26\rho_s$ and the time step to $0.07a/c_s$. The main ions are sampled by about 100 markers per grid. The numbers of electron and carbon markers are half the number of the ion markers. To obtain quasi-steady-state nonlinear simulations, we apply a Krook-type source given by

$$S_{E\sigma}(x, \theta, \zeta, v_\parallel, \mu_\sigma) = -\gamma_{\rm src}\delta F_\sigma(x, E_\sigma), \tag{15}$$

which is similar to the source operator in Ref. 27. The coefficient $\gamma_{\rm src}$ is set to around 2% of the maximum linear growth rate. The fixed (Dirichlet) boundary condition is imposed for non-zonal potential fluctuations at both the inner and outer boundaries of the radial simulation domain ($\delta\phi_{n\neq0} = 0$), as well as for the zonal potential at the outer boundary. For the zonal potential at the inner boundary, we impose the Neumann boundary condition of $\partial\delta\phi_{n=0}/\partial x = 0$. In order to prevent unphysical profile evolution near the boundaries, we also designate buffer zones where fluctuations are enforced to damp by a Krook operator. Each of the inner and outer buffer zones stretches for about 20% of the whole simulation domain from their neighboring boundaries toward the domain's center. Figure 4 shows the T_e profile (black curve) used in the baseline simulation setup and illustrates the radial domain configuration (black arrow and shaded zones). The inner and outer buffer zones are located in close proximity to the plasma gradient region. In this case, the physical domain except the buffer zones, whose extent is denoted by D, is the same as the plasma gradient region, i.e., $W = D = 0.1$.

Since the most CGYRO simulations in Ref. 22 include both $E_{r,eq}$ and fast ions, we revise them by excluding these two factors. The numerical parameters used in CGYRO simulations are as follows: The radial and binormal box sizes are $L_x = 135.5\rho_s$ and $L_y = 93.8\rho_s$, respectively. Resolutions are $(n_x, n_\theta, n_\zeta) = (216, 56, 16)$ for radial, poloidal, and toroidal grids and $(n_E, n_\xi) = (8, 24)$ for energy and pitch angle grids. For a more solid benchmark, we add results from another flux-tube code GENE,[6] adopting the same simulation condition.

Figure 5 shows linear growth rate γ and angular frequency ω spectra obtained from two gKPSP versions with the BK electron models
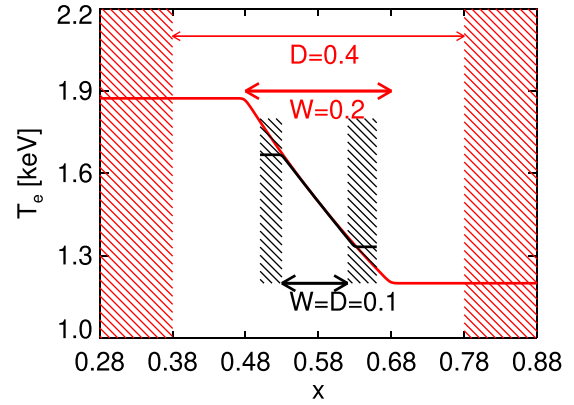

FIG. 4. Radial profiles of electron temperature T_e imported into simulations with $W = D = 0.1$ (black) and $W = 0.2$ along with $D = 0.4$ (red). The plasma gradient region width W and the physical domain size D are represented by the thick and thin arrows, respectively. The buffer zones are represented by the shaded regions.

based on the analytic (blue) and numerical magnetic geometries (red). We also present the results from CGYRO (black) and GENE (green), which are almost identical. Negative frequencies correspond to modes propagating in the electron diamagnetic drift direction. While the differences between the results from the analytic BK and gyrokinetic electron models are noticeable, the extended BK electron model improves the agreement with the gyrokinetic electron model to a satisfactory level. This implies that if general tokamak magnetic geometries are taken into account correctly, under conditions where the BK electron model can be applied, it can quantitatively reproduce outputs from the full gyrokinetic simulations. In the previous analysis,[22] the unstable electron mode was found to be a kind of collisionless TEM by scrutinizing the dependencies of the linear growth rate on electron density and temperature gradients, as well as collisions. It is remarkable that the absolute value of the mode frequency decreases with the wavenumber for $k_\theta \rho_s > 0.3$. This behavior is distinguished from a typical drift wave frequency spectrum, which increases with $k_\theta \rho_s$. The impurity content and the shaped magnetic geometry may result in the distinct linear
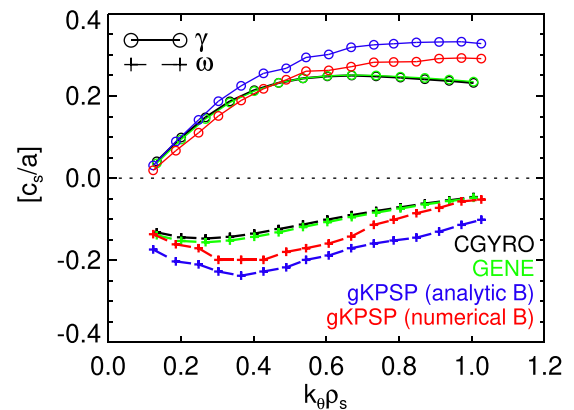

FIG. 5. Linear growth rates γ and frequencies ω as a function of $k_\theta \rho_s$ from different codes. The gKPSP simulations use the plasma gradient region width $W = 0.1$ with the same physical domain size $D = W$.

spectrum. We defer a more detailed study of underlying physics of the simulated instability to a subsequent paper. In spite of the overall agreement among the codes, discrepancies still remain in the growth rates at $k_\theta \rho_s > 0.6$ and the frequencies around $k_\theta \rho_s \sim 0.5$. Those are possibly because of the approximations in our BK electron model such as the omissions of the perpendicular magnetic drift (zero orbit width) and neoclassical polarization of trapped electrons, the adiabatic response of passing electrons, etc. The differences between local and global simulations can also cause the discrepancies.
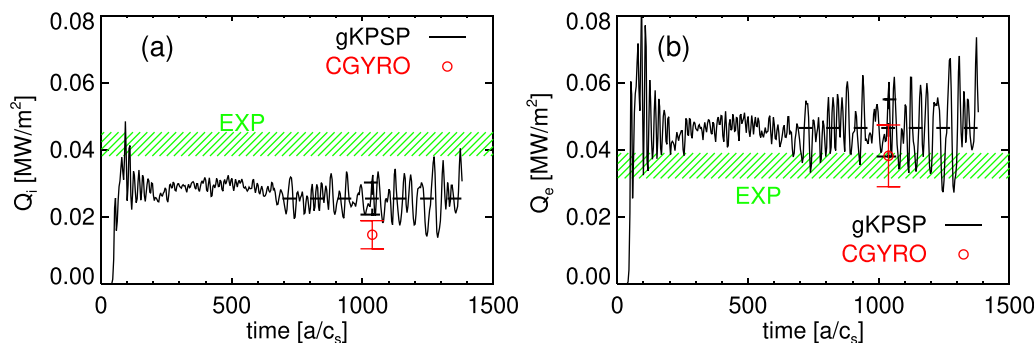
Figure 6 shows time histories of ion and electron heat fluxes computed from a nonlinear gKPSP simulation with $W = D = 0.1$. The local heat fluxes are obtained by the radial average around x_{ref} ($0.55 \le x \le 0.61$). We display the averaged heat fluxes over the last half of the simulation time by the black dashed lines. The red circles represent the mean heat fluxes from a nonlinear CGYRO simulation, obtained by time average of a quasi-steady state. The corresponding standard deviations are indicated by the error bars. In this baseline case, the gKPSP simulation predicts the average ion heat flux 70% larger than that from CGYRO and the mean electron heat flux to exceed the CGYRO result by only 20%.

Although the present study does not aim to match the experimental heat transport levels, it is meaningful to compare the nonlinear simulation results with the experiment. The experimental heat fluxes as well as their uncertainties have been estimated by the previous power balance analysis combined with the random data sampling and the error propagation technique.[22] Those results are displayed by the green shaded bands in Fig. 6. In the perspective of turbulent transport theories, it is useful to quantify the heat transport levels induced by the gyro-Bohm diffusivity given by $\chi_{\mathrm{gB}} = \rho_s^2 c_s / a$. Defining $Q_{\mathrm{gB},\sigma} = \chi_{\mathrm{gB}} n_\sigma T_\sigma / a$, we have $1 Q_{\mathrm{gB,i}} = 0.039\,\mathrm{MW/m^2}$ and $1 Q_{\mathrm{gB,e}} = 0.036$ $\mathrm{MW/m^2}$ at $x = x_{\mathrm{ref}}$ for ions and electrons, respectively. Therefore, experimental heat fluxes are approximately $\sim 1 Q_{\mathrm{gB},\sigma}$ for both ions and electrons. Given the presumed impurity profile and the omission of fast ions, the gKPSP and CGYRO simulation results occasionally agree with the experimental electron heat flux, but they underestimate the ion transport level. The previous validation study has identified information of impurities and fast ions as necessary input data for a clearer conclusion.[22] By securing the required experimental data, we will continue validation efforts for KSTAR plasmas in the future.

We examine influences from the radial domain size on turbulent transport levels by carrying out additional nonlinear gKPSP simulations with wider plasma gradient regions. In addition to numerical damping near the inner and outer boundaries, it is well known that in global gyrokinetic simulations, turbulent transport is strongly affected by the width of the unstable region.[28,29] To distinguish these two effects, we vary the plasma gradient region width W with two different setups for the physical domain size D. One approach involves setting $D = W$, corresponding to the inner and outer buffer zones in close proximity to the plasma gradient region. The other method does fixing $D = 0.4$, i.e., the distant buffer zones for the narrower $W \le 0.3$. The two domain configurations are illustrated in Fig. 4. In order to avoid strong fluctuations excited by the large gradients in the experimental plasma profiles at $x > 0.65$, we modify the experimental density and temperature profiles of all the plasma species. The profiles are enforced to have a constant inverse gradient scale length over the whole radial domains for the cases with $W \ge 0.2$. We set the constant $1/\Lambda_Y$ to be equal to the values at x_{ref}. These profile modifications make $1/\Lambda_Y$ at inner radii larger than the original experimental values.

In linear simulations with different W, the growth rates and frequencies of the modes with $k_\theta \rho_s > 0.5$, measured at x_{ref}, are almost identical. With the wide $W > 0.2$, the modes with low $k_\theta \rho_s < 0.5$ show some changes: The structures of the low-k modes expand to inner radii at $x < 0.5$. The growth rates around $k_\theta \rho_s \sim 0.4$ increase by 20%–30% compared to those in the $W = 0.1$ case and thus the linear flux-tube simulations. The increased growth rates of the $k_\theta \rho_s \sim 0.4$ modes may lead to modest raises in the heat fluxes with $W > 0.2$. From nonlinear simulations with different W and D, we obtain the radial profiles of the ion and electron heat fluxes in Fig. 7. The heat fluxes are averaged over the time period denoted by the dashed lines in Fig. 6. As W increases, the height and width of the heat flux profiles increase simultaneously. In the $D = W$ cases (the thin curves), the numerical damping from the nearby buffer zones yields the more reduced heat fluxes compared to the cases with the distant buffers ($D = 0.4$).

Figure 8 shows the volume-averaged heat fluxes as functions of the ratio of the plasma gradient region width to the mode radial correlation length W/l_{corr}. The radial average window ($0.55 \le x \le 0.61$) is the same as that in Fig. 6. Here, we estimate the radial correlation length l_{corr}, defined as the full width of radial mode structures, by measuring the width of the radial wavenumber power spectra of $\delta\phi$

FIG. 6. Time histories of heat fluxes of ions (a) and electrons (b) from a nonlinear gKPSP simulation with the plasma gradient region width $W = 0.1$ and the same physical domain size $D = W$. Heat fluxes obtained from a CGYRO simulation are shown by the red symbols. The error bars represent the standard deviations of the time averages. The power balance analysis results in Ref. 22 are displayed by the green shaded bands.
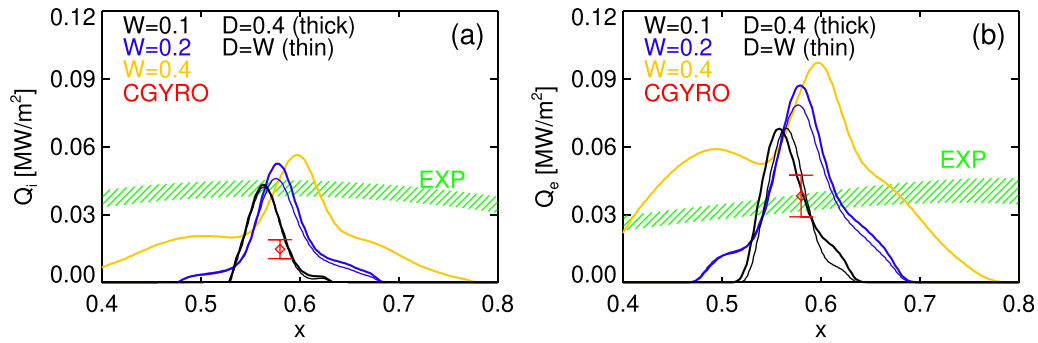
FIG. 7. Radial profiles of heat fluxes of ions (a) and electrons (b) from nonlinear gKPSP simulations with different values of the plasma gradient region width W and the physical domain size D. Heat fluxes obtained from a CGYRO simulation are shown by the red symbols with the error bars. The power balance analysis results in Ref. 22 are displayed by the green shaded bands.
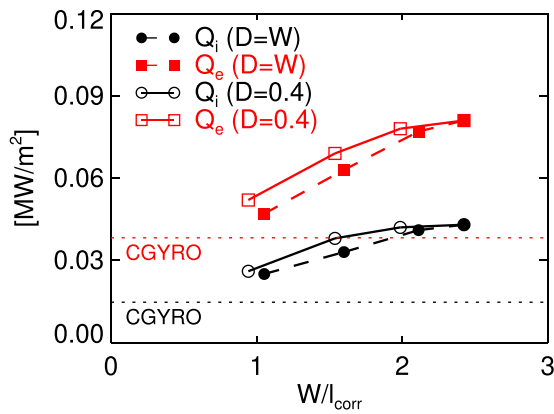
FIG. 8. Volume-averaged ion (black) and electron (red) heat fluxes as functions of W/l_{corr} from gKPSP simulations with two different settings of the physical domain size D. Heat fluxes obtained from a CGYRO simulation are shown by the dotted lines.

fluctuation. The average l_{corr} values for the time interval of $20\,a/c_s$ during the nonlinear saturation are listed in Table I. The plasma gradient region width of $W = 0.1$, which corresponds to $17\rho_s$, is slightly narrower than the mode correlation length $l_{corr} \geq 20\rho_s$ in the wider W cases. Regardless of the D conditions, the ion and electron heat fluxes increase with increasing W/l_{corr}, being consistent with the previous result, which reports the proportional relation between turbulent transport and W for $W < 200\rho_s$.[29] For the same W values, the heat fluxes with $D = W$ (the filled symbols) are more reduced than the $D = 0.4$ cases (the open symbols). However, the heat flux differences

TABLE I. Radial mode correlation lengths for different values of the plasma gradient region width W and the physical domain size D.

	W			
	0.1	0.2	0.3	0.4
$D = W$	$16\rho_s$	$21\rho_s$	$24\rho_s$	$28\rho_s$
$D = 0.4$	$18\rho_s$	$22\rho_s$	$26\rho_s$	$28\rho_s$

between the two D setups are much smaller than the variations among the different W cases. Specifically, compared to the largest Q_e in the $W = D = 0.4$ case, Q_e with $W = D = 0.1$ decreases by 58% and Q_e in the case with $W = 0.1$ and $D = 0.4$ is similarly reduced by 64%. This manifests that the numerical damping effect does not contribute substantially to the reduced turbulent transport at small W/l_{corr}. In the gKPSP simulation with $W = D = 0.4$, the ion and electron heat fluxes are, respectively, 3 times and 2 times larger than those from the CGYRO simulation. This suggests that our BK electron model overestimates turbulent transport compared to the gyrokinetic model. The approximations employed in our BK model are likely to cause the overestimation. However, the case with $W = 0.4$ is very unlikely to correspond to the flux-tube limit, although global simulations with larger W/ρ_s may produce results more similar to the flux-tube limit. We need to identify the heat flux differences between global and flux-tube simulations, differentiating them from the overestimation caused by our BK model. The differences between global and flux-tube results can be attributed to nonlinear mesoscale phenomena as well as linear instabilities altered by the global profile variation. We will discuss impacts of nonlinear mesoscale phenomena in global simulations shortly. To clarify sources of the discrepancies between the gKPSP and CGYRO results in Fig. 8, further validation studies against global full gyrokinetic simulations are required.

It is instructive to compare Fig. 8 with the scan of the width of the strong T_i gradient region in Fig. 3 in Ref. 29. First of all, we note that our simulation condition is quite different from that of Ref. 29, which is a deuterium–electron plasma of $T_i = T_e$ with an analytic concentric circular magnetic geometry. In Ref. 29, the adiabatic electron response is assumed, and only ITG turbulence is examined. In this work, we consider an experimental multi-species plasma and kinetic electrons by using the BK model. Despite these distinct simulation conditions, for small $W/\rho_s < 200$, the dependencies of turbulent transport on W are consistent: Both the heat diffusivity χ in Ref. 29 and Q_e as well as Q_i in Fig. 8 significantly increase with $1/\rho^*_{eff} = W/\rho_s$. For large $W/\rho_s \geq 200$, the transport induced by global ITG turbulence in Ref. 29 converges to the flux-tube result. The convergence is expected to occur around $W/\rho_s \sim 200$ since χ with $W/\rho_s \sim 220$ is close to the flux-tube limit. On the other hand, in our W scan with $D = 0.4 \approx 70\rho_s$ in Fig. 8, the increments in the heat fluxes are likely to be saturated at the largest W/l_{corr} value

($W \approx 70\rho_s$). However, we cannot rule out the impact of the nearby buffer zones restricting the turbulent transport in the $W = 0.4$ case. We note that the buffers in our simulations are placed close to the turbulent region compared to the setting in Ref. 29. Although it is desirable to obtain heat fluxes clearly saturated at sufficiently large W/ρ_s, the largest W is limited to $W \leq 100\rho_s$ in the present experimental plasma condition. It is valuable to study the effects of the width of the strong gradient region on transport in global TEM turbulence. This study will be facilitated in a simplified plasma condition and magnetic geometry, rather than in an experimental plasma.

The mechanism behind the transport reduction in narrow turbulent regions is still not fully understood. It has been reported from a device size scaling study, the linear growth rates are similar for different plasma size a/ρ_i.[28] Therefore, the reduction in transport at small W values is conventionally recognized as a consequence of nonlinear mesoscale processes. An initially invoked mechanism is turbulence spreading,[30] by which fluctuation excited in the unstable region diffuses into the adjacent, linearly stable region by mode-mode coupling. As the width of the driving region decreases, the stabilizing effect of spreading becomes more pronounced. Recently, a global gyrokinetic simulation study has identified two distinguished mechanisms for the generation of zonal flows depending on the width of the unstable region.[31] When W is much wider than the mode correlation length l_{corr}, an incoherent zonal flow is driven, and its modulational growth is prohibited. With a narrow unstable region of $W \sim l_{corr}$, a coherent zonal flow is efficiently amplified by the modulational instability, leading to a turbulence saturation level lower than those in the wide W cases. These findings in zonal flow generation can also explain the reduction in transport at small W values. Crucial mechanisms causing the transport reduction may be uncovered by quantifying their contributions on transport levels for different W.

V. GLOBAL SIMULATIONS WITH A WIDE EXPERIMENTAL PLASMA GRADIENT REGION

To explore features of global simulations using the experimental magnetic geometry and plasma profiles, we take the experimental plasma profiles in Fig. 3 without any modification. We set the plasma gradient region as $x = 0.38 - 0.63$, denoted by the black arrows in Fig. 3, and place the buffer zones next to the plasma gradient region, i.e., $W = D = 0.35$. This wide domain embraces the $W = D = 0.1$ domain of the benchmark work in Sec. IV. It is of interest to inquire

how turbulent heat fluxes distribute within the wide radial region. Except the radial domain, we use the same simulation parameters with the previous benchmark work: To maintain the radial resolution and marker number density, we increase the numbers of radial grid points and markers accordingly. In this section, we use the ion thermal velocity at the magnetic axis $v_{Ti0} \equiv \sqrt{T_i(0)/m_i}$ as a unit of velocity.

In linear simulations with the wide experimental plasma gradient region, the unstable modes reside in the outer radii $x > 0.55$. The growth rate and frequency spectra, measured at $x = x_{\text{ref}}$, are almost identical to the results with $W = D = 0.1$ in Fig. 5. In a quasi-steady state of a nonlinear simulation using the experimental profiles, the radial profiles of ion and electron heat fluxes are obtained. This is done by time-averaging over the last half of the quasi-steady-state period, which is similar to that in the localized simulation in Fig. 6. The heat flux profiles are shown by the black, solid curves in Fig. 9. The results with $W = D = 0.1$ in the validation work in Fig. 7 are duplicated by the red curves for comparison. The simulation with the wide experimental plasma gradient region yields the heat fluxes larger than those in the $W = D = 0.1$ simulation, as expected from the sensitivity study against the width of the plasma gradient region in Fig. 7. It is noticeable that despite the wide turbulent region, the heat fluxes concentrate in the outer region and significantly decrease in the inner zone of $x < 0.5$.

To inspect linear instabilities and transport levels in the inner zone, we perform supplementary simulations with a narrow plasma gradient region focused on the inner radii $x = 0.38 - 0.48$, which is indicated by the cyan arrows in Fig. 3, and $D = W = 0.1$. Figure 10 shows the growth rate and frequency spectra from linear simulations of gKPSP and CGYRO, confirming reasonable agreement again. The maximum growth rate is about 30% of that of the results with the outer region only in Fig. 5, considering a unit conversion factor $c_s(0.58)/v_{Ti0} = 0.82$. The sign of the mode frequency changes from negative to positive as k_y increases above $k_\theta\rho_{i0} > 0.5$, suggesting a transition from TEM to a mode propagating in the ion-diamagnetic drift direction. The nonlinear simulation localized in the inner radii predicts finite heat fluxes corresponding to about 30% of the outer regions, as shown by the blue curves in Fig. 9. This implies that the heat flux profiles with the wide plasma gradient region are not a simple superposition of the local fluxes from the two independent simulations restricted to either the inner or the outer region.
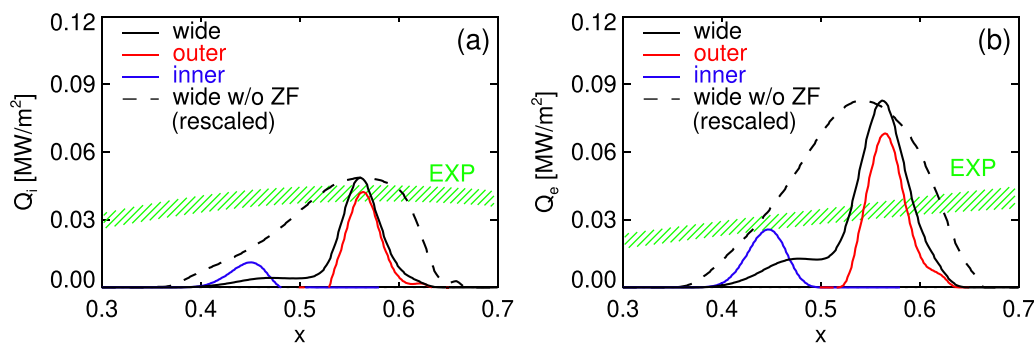
FIG. 9. Radial profiles of heat fluxes of ions (a) and electrons (b) from nonlinear gKPSP simulations employing different plasma gradient regions. Heat fluxes from a simulation artificially removing the zonal flow, shown by the dashed curves, are rescaled for comparison. The rescale factors are 0.25 and 0.21 for the ion and electron heat fluxes, respectively. The power balance analysis results in Ref. 22 are displayed by the green shaded bands.
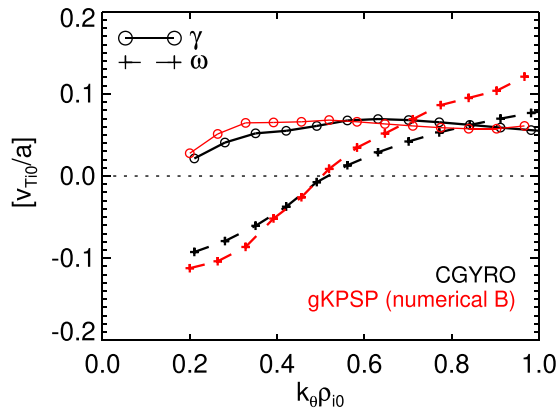
FIG. 10. Linear growth rate and frequency spectra from gKPSP and CGYRO simulations at $x = 0.43$.

The concentration of the turbulent fluxes in the outer region can be understood in the context of mesoscale transport phenomena in global simulations. In what follows, we present the dynamic coupling of turbulence spreading and the zonal flow in the simulation with the wide experimental plasma gradient region. Since the modes in the outer region have much higher growth rates than the inner modes, turbulence in the outer region reaches the local saturation level much earlier than fluctuations in the inner zone. Figure 11(a) shows time evolution of turbulence intensity profiles during the early stage of the nonlinear saturation. The turbulence in the strong driving (outer) region spreads into the weakly unstable (inner) radii. It should be noted that turbulence always accompanies a zonal flow. The zonal flow profile at the nonlinear saturation phase around $t \sim 100a/v_{Ti0}$ is displayed by the thin black curve in Fig. 11(b). The zonal flow expands into the inner region before the inner region turbulence reaches to a finite saturation level. We note that in the simulation with the inner region only, the nonlinear saturation of turbulence occurs around $t = 200a/v_{Ti0}$. Consequently, a considerable level of the zonal flow is induced by turbulence spreading even away from the strong turbulent region. The time-averaged zonal flow profile over the quasi-steady state is shown by the thick black curve in Fig. 11(b). The zonal flow

keeps its structure constant after the saturation time. We estimate the zonal flow shear defined by[32]

$$\omega_{ZF} \equiv \frac{(RB_p)^2}{B} \frac{\partial^2}{\partial \psi^2} \delta \phi_{00},$$

at the outer mid-plane, and plot it by the red curves in Fig. 11(b). Here, $\delta \phi_{00}$ is the zonal component of $\delta \phi$. In the inner region, the zonal flow shear is comparable to the maximum local linear growth rate of the inner modes [the red line in Fig. 11(b)]. These observations suggest that the inner modes are saturated by the zonal flow accompanied by turbulence spreading from the outer region.

To confirm this effect of the zonal flow, we carry out a simulation artificially removing the zonal flow. The heat fluxes from the simulation without the zonal flow are shown by the dashed curves in Fig. 9. Because the absence of the zonal flow largely elevates turbulence and transport levels, we rescale the heat flux profiles to pay attention to their shapes. Unlike the case with the zonal flow, the heat fluxes are broadly distributed in the whole turbulent region. Particularly, the rescaled heat fluxes in the no zonal flow simulation have the shapes similar to a superposition of the localized fluxes from the two simulations with the zonal flows, each considering either the inner or the outer region only. This manifests that in the present simulation condition, the zonal flow reinforces the concentration of the turbulent fluxes into the strong driving region by suppressing turbulence in the weakly unstable region. To clarify underlying mechanisms of this observation, detailed analyses of fluctuations and zonal flow generation are necessary, which, however, are beyond the scope of this work.

Although our results are physically valid under the present simulation condition, its caveat is that the way the zonal flow organizes radial turbulent flux profiles depends on plasma physics parameters and their radial profiles. Turbulence spreading is usually supposed to broaden fluctuation intensity and thus turbulent flux profiles, as observed in previous simulation studies.[33–35] However, the characteristics of turbulence in our simulation condition are distinguished from those in the previous works. The previous numerical studies of turbulence spreading consider turbulence excited from one type of micro-instability that is ITG in most cases. On the other hand, our experimental plasma is predicted to be unstable for the different types of microinstabilities at the distant radii. Those are, respectively, the
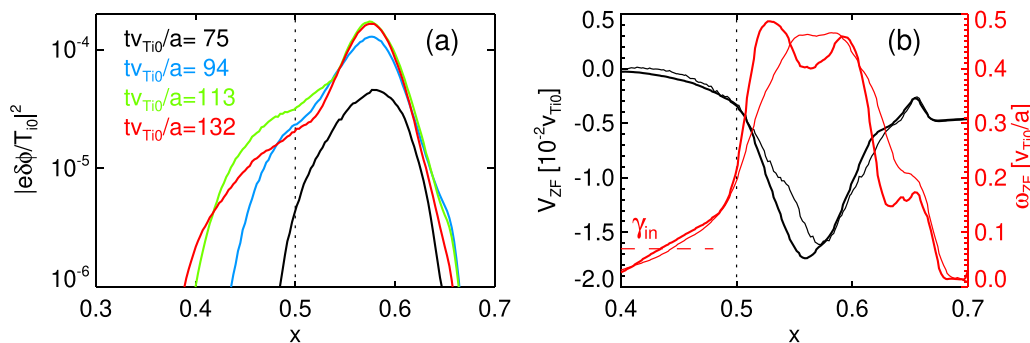

FIG. 11. (a) Time evolution of the radial profile of the perturbed potential intensity. (b) Radial profiles of a zonal flow (black) and its shear (red). The profiles at the early saturation phase ($tv_{Ti0}/a = 100$) and the quasi-steady state are shown by the thin and thick curves, respectively. The vertical lines indicate a rough border between the weakly unstable inner and strongly driving outer regions.

TEM and TEM-ion mode mixture in the outer and inner regions (Figs. 5 and 10). The generation of zonal flows can be influenced by the constitution of fluctuations. For example, a previous simulation study reported that the potential intensity ratio of zonal to non-zonal modes substantially increases as the type of turbulence changes from TEM to ITG.[12] This suggests that a dynamic coupling of turbulence spreading and a zonal flow in ITG-TEM mixed turbulence is different from mesoscale transport dynamics in pure ITG turbulence. In this regard, it is worth mentioning that the relations between turbulence spreading and zonal flows are still not fully understood. A previous theory reported that zonal flows may promote turbulence spreading.[36] On the contrary, another concluded that zonal flows are not the predominant agents of spreading,[37] anticipating concurrent spreading of turbulence and a zonal flow.

Assuming the constant $Z_{\text{eff}} = 2.0$ profile, the gKPSP simulation predicts that the heat fluxes are concentrated in the outer region, which are not apparent in the experimental profiles. Density profiles of the ion species have a strong influence on types of microinstabilities excited in different radial regions in addition to their linear growth rates. Considering the complex coupling of turbulence spreading and a zonal flow in multi-mode turbulence, vast uncertainty in density profiles of the ion species implies that very diverse radial profiles of turbulent transport can be produced in our simulations. Therefore, we cannot yet claim the validity of our BK electron model against the experimental results considered.

The spatial patterns of zonal flows and turbulent fluxes can be affected by numerical boundary conditions. In this work, we adopt the conventional boundary condition described in Sec. IV, which oversimplifies physics in edge and open-field line regions. Simulation studies incorporating more realistic models for the open-field line region have uncovered the distinguished behaviors of peripheral turbulent plasmas and edge-core coupling.[38,39] We note that our findings can be changed by applying different edge models. However, to the best of our knowledge, there has been no report of zonal flows, accompanied by turbulence spreading from a strong driving region, suppressing turbulence in weakly unstable regions.

VI. CONCLUSION AND DISCUSSION

We have extended the BK electron model in the gKPSP code for its application in experimental magnetic geometries. The updated BK model is validated against the gyrokinetic electron model in the flux-tube codes, CGYRO and GENE. From the comparisons among the simulations based on the local parameters of the KSTAR L-mode plasma, we confirm a reasonable agreement among the linear results from the different codes, albeit some discrepancies still remain. In the nonlinear gKPSP simulation with the narrow plasma gradient region whose width comparable to the mode correlation length, the ion and electron heat fluxes are compatible with those calculated by CGYRO. However, with the unstable region sufficiently wider than the mode correlation length, the nonlinear gKPSP simulation predicts the turbulent heat fluxes 2–3 times larger than those from CGYRO. Taking into account the differences between the flux-tube and global simulations, the overall level of agreement is satisfactory, encouraging further development of the BK electron model. In addition, we have studied inherent features of global simulations by using the wide range of the experimental plasma profiles. In the present KSTAR plasma parameters, the different types of microinstabilities are predicted to be unstable at the distant radii. The

dynamical coupling of turbulence spreading and the zonal flow leads to the turbulent fluxes localized to the strong driving region, which contrasts with the effect of turbulence spreading in the previous works. This demonstrates that mesoscale transport phenomena impact on turbulent fluxes in various ways depending on plasma parameters, calling for a careful interpretation of global simulation results.

In future works, we will aim for more improved validation results of the BK electron model. To this end, the BK electron model needs to be more extended by incorporating effects of the finite orbit width of trapped electrons and the corresponding neoclassical polarization. Though the BK equations including the finite orbit width effects are present,[3] the more accurate equations are difficult to evaluate in experimental magnetic geometries. A practical solution is to calculate the unperturbed orbit from the drift-kinetic equations numerically and to use the orbit points in the calculations of the action and the bounce average. The gyrokinetic Poisson equation also necessitates modification through the inclusion of the neoclassical polarization charge density of tapped electrons. For passing electrons, a new kinetic model is under development by defining the action-angle variables associated with their periodic transit motions. This establishes an unified description of the total electrons in an orbit-averaged kinetic formalism. Another prerequisite for more improved validation studies is experimental plasma equilibrium data with well-diagnosed kinetic profiles and impurity contents as well as fluctuations. Ohmic L-mode discharges are very relevant to be analyzed by using the BK electron model. To discern discrepancies between the BK and gyrokinetic electron models, global simulations employing the full gyrokinetic description are required as benchmark data.

AUTHOR DECLARATIONS
Conflict of Interest

The authors have no conflicts to disclose.

Author Contributions

Sumin Yi: Conceptualization (lead); Data curation (lead); Investigation (lead); Software (lead); Validation (lead); Writing – original draft (lead). **Lei Qi:** Software (supporting). **Choongki Sung:** Conceptualization (supporting); Data curation (equal); Investigation (equal); Validation (equal). **E.S. Yoon:** Data curation (equal); Investigation (equal); Validation (equal). **Jae-Min Kwon:**

DATA AVAILABILITY

The data that support the findings of this study are available from the corresponding author upon reasonable request.

APPENDIX: NUMERICAL CALCULATION OF HAMILTONIAN $H_0(\psi, J, \mu_e)$

We set a uniform grid (x_i, J_l, μ_k). Here, $X_i = X_0 + i\Delta_X$ for an index i running from 0 to N_X, where X stands for either x, J, or μ. The Hamiltonian is expressed as

$$H_0(x, J, \mu_e) = \sum_{i,l,k} \hat{H}_{0,ilk} C_i(x) C_l(J) L_k(\mu_e), \tag{A1}$$

where C_i and L_k are, respectively, the cubic and linear spline functions centered at ith and kth grid points, defined as[40]

$$C_i(X) = \frac{1}{6} \begin{cases} \dfrac{(X - X_{i-2})^3}{\Delta_X^3}, & \text{if } X_{i-2} < X \leq X_{i-1} \\[2mm] 1 + 3\dfrac{X - X_{i-1}}{\Delta_X} + 3\dfrac{(X - X_{i-1})^2}{\Delta_X^2} - 3\dfrac{(X - X_{i-1})^3}{\Delta_X^3}, & \text{if } X_{i-1} < X \leq X_i \\[2mm] 1 + 3\dfrac{X_{i+1} - X}{\Delta_X} + 3\dfrac{(X_{i+1} - X)^2}{\Delta_X^2} - 3\dfrac{(X_{i+1} - X)^3}{\Delta_X^3}, & \text{if } X_i \leq X < X_{i+1} \\[2mm] \dfrac{(X_{i+2} - X)^3}{\Delta_X^3}, & \text{if } X_{i+1} \leq X < X_{i+2} \\[2mm] 0, & \text{otherwise,} \end{cases} \tag{A2}$$

and

$$L_k(X) = \begin{cases} \dfrac{X - X_{i-1}}{\Delta_X}, & \text{if } X_{i-1} < X \leq X_i \\[2mm] \dfrac{X_{i+1} - X}{\Delta_X}, & \text{if } X_i \leq X < X_{i+1} \\[2mm] 0, & \text{otherwise.} \end{cases} \tag{A3}$$

At the grid points, the H_0 values are given by

$$H_0(x_i, J_l, \mu_k) = \mu_k B_{min}(x_i) + \frac{m_e}{2} u_{bc}^2(x_i, J_l, \mu_k), \tag{A4}$$

where the unknown u_{bc} satisfying $J(\psi_i, u_{bc}, \mu_k) = J_l$ is obtained by a root finding method. From Eqs. (A1) and (A4), we comprise the following matrix equation:

$$\sum_{i',j'} C_{i'}(x_i) C_{l'}(J_l) \hat{H}_{0,i',l',k} = H_0(x_i, J_l, \mu_k), \tag{A5}$$

where

$$C_{i'}(x_i) = \frac{1}{6} \begin{cases} 4 & \text{for} & i' = i \\ 1 & \text{for} & i' = i \pm 1 \\ 0, & \text{otherwise.} \end{cases} \tag{A6}$$

We determine the coefficient $\hat{H}_{0,ilk}$ by solving the matrix equation with the boundary condition of vanishing second derivatives. From the radial differentiation of Eq. (A1), we obtain

$$\frac{\partial H_0(x, J, \mu_e)}{\partial x} = \sum_{i,l,k} \hat{H}_{0,ilk} \frac{\partial C_i(x)}{\partial x} C_l(J) L_k(\mu_e). \tag{A7}$$

REFERENCES

[1]T. S. Hahm, Phys. Fluids **31**, 2670 (1988).

[2]A. J. Brizard and T. S. Hahm, Rev. Mod. Phys. **79**, 421 (2007).

[3]R. G. Littlejohn, Phys. Scr. **T2**(1), 119 (1982).

[4]B. H. Fong and T. S. Hahm, Phys. Plasmas **6**, 188 (1999).

[5]J. Candy, E. A. Belli, and R. V. Bravenec, J. Comput. Phys. **324**, 73 (2016).

[6]F. Jenko, W. Dorland, M. Kotschenreuther, and B. N. Rogers, Phys. Plasmas **7**, 1904 (2000).

[7]R. Hager, S. Ku, A. Y. Sharma, C. S. Chang, R. M. Churchill, and A. Scheinberg, Phys. Plasmas **29**, 112308 (2022).

[8]Y. Idomura, S. Tokuda, and Y. Kishimoto, J. Plasma Fusion Res. **6**, 17 (2004), available at https://www.jspf.or.jp/JPFRS/PDF/Vol6/jpfrs2004_06-017.pdf.

[9]L. Qi, J. Kwon, T. S. Hahm, and G. Jo, Phys. Plasmas **23**, 062513 (2016).

[10]J.-M. Kwon, L. Qi, S. Yi, and T. S. Hahm, Comp. Phys. Commun. **215**, 81 (2017).

[11]L. Qi, J.-M. Kwon, T. S. Hahm, S. Yi, and M. J. Choi, Nucl. Fusion **59**, 026013 (2019).

[12]L. Qi, J.-M. Kwon, H. Jhang, T. S. Hahm, and M. Leconte, Nucl. Fusion **60**, 036009 (2020).

[13]P. W. Terry, M. Greenwald, J.-N. Leboeuf, G. R. McKee, D. R. Mikkelsen, W. M. Nevins, D. E. Newman, D. P. Stotler, and Task Group on Verification and Validation, Phys. Plasmas **15**, 062503 (2008).

[14]P. H. Diamond, S.-I. Itoh, K. Itoh, and T. S. Hahm, Plasma Phys. Controlled Fusion **47**, R35 (2005).

[15]T. S. Hahm and P. H. Diamond, J. Korean Phys. Soc. **73**, 747 (2018).

[16]J. Abiteboul, T. Görler, F. Jenko, D. Told, and ASDEX Upgrade Team. Phys. Plasmas **22**, 092314 (2015).

[17]A. B. Navarro, D. Told, F. Jenko, T. Görler, T. Happel, and ASDEX Upgrade Team. Phys. Plasmas **23**, 042312 (2016).

[18]G. Merlo, Z. Huang, C. Marini, S. Brunner, S. Coda, D. Hatch, D. Jarema, F. Jenko, O. Sauter, and L. Villard, Plasma Phys. Controlled Fusion **63**, 044001 (2021).

[19]Y. J. Kim, J.-M. Kwon, L. Qi, and T. S. Hahm, Phys. Plasmas **29**, 042103 (2022).

[20] R. Roy and F. W. J. Oliver, "Elementary functions," in *NIST Handbook of Mathematical Functions* (Cambridge University Press, Cambridge, 2010), Chap. 4.

[21] L. Wang and T. S. Hahm, Phys. Plasmas **16**, 062309 (2009).

[22] D. Kim, J. Kang, M. W. Lee, J. Candy, E. S. Yoon, S. Yi, J.-M. Kwon, Y-c Ghim, W. Choe, and C. Sung, Curr. Appl. Phys. **42**, 60 (2022).

[23] T. Görler, N. Tronko, W. A. Hornsby, A. Bottino, R. Kleiber, C. Norscini, V. Grandgirard, F. Jenko, and E. Sonnendrücker, Phys. Plasmas **23**, 072503 (2016).

[24] S. Satake, M. Nataka, T. Pianpanit, H. Sugama, M. Nunami, S. Matsuoka, S. Ishiguro, and R. Kanno, Comp. Phys. Commun. **255**, 107249 (2020).

[25] Z. Lin, W. M. Tang, and W. W. Lee, Phys. Plasmas **2**, 2975 (1995).

[26] J. Seo, H. Jhang, and J.-M. Kwon, Phys. Plasmas **29**, 052502 (2022).

[27] B. F. McMillan, S. Jolliet, T. M. Tran, L. Villard, A. Bottino, and P. Angelino, Phys. Plasmas **15**, 052308 (2008).

[28] Z. Lin, S. Ethier, T. S. Hahm, and W. M. Tang, Phys. Rev. Lett. **88**, 195004 (2002).

[29] B. F. McMillan, X. Lapillonne, S. Brunner, L. Villard, S. Jolliet, A. Bottino, T. Görler, and F. Jenko, Phys. Rev. Lett. **105**, 155001 (2010).

[30] T. S. Hahm, P. H. Diamond, Z. Lin, K. Itoh, and S.-I. Itoh, Plasma Phys. Controlled Fusion **46**, A323 (2004).

[31] S. Yi, H. Jhang, S. S. Kim, and J.-M. Kwon, Nucl. Fusion **62**, 076037 (2022).

[32] T. S. Hahm and K. H. Burrell, Phys. Plasmas **2**, 1648 (1995).

[33] T. S. Hahm, P. H. Diamond, Z. Lin, G. Rewoldt, Ö. D. Gürcan, and S. Ethier, Phys. Plasmas **12**, 090903 (2005).

[34] S. Yi, J.-M. Kwon, P. H. Diamond, and T. S. Hahm, Phys. Plasmas **21**, 092509 (2014).

[35] S. Yi, J.-M. Kwon, P. H. Diamond, and T. S. Hahm, Nucl. Fusion **55**, 092002 (2015).

[36] L. Chen, R. B. White, and F. Zonca, Phys. Rev. Lett. **92**, 075004 (2004).

[37] Ö. D. Gürcan, P. H. Diamond, and T. S. Hahm, Phys. Plasmas **13**, 052306 (2006).

[38] C. S. Chang, S. Ku, G. R. Tynan, R. Hager, R. M. Churchill, I. Cziegler, M. Greenwald, A. E. Hubbard, and J. W. Hughes, Phys. Rev. Lett. **118**, 175001 (2017).

[39] G. Dif-Pradalier, P. Ghendrih, Y. Sarazin, E. Caschera, F. Clairet, Y. Camenen, P. Donnel, X. Garbet, V. Grandgirard, Y. Munschy, L. Vermare, and F. Widmer, Commun. Phys. **5**, 229 (2022).

[40] P. M. Prenter, *Splines and Variational Methods* (Wiley, New York, 1975), Chap. 4.

04 March 2024 04:47:30